Numerical and Experimental Investigation of Float Shape Effects on Single-Heaving Wave Energy Converter Performance

Reza Abbasi, James Harris, Lachlan Stedman, Tom Baldock

Abstract—**This study presents a geometric design procedure for the buoy of a single-body wave energy converter (WEC) based on specific incident wave characteristics, utilizing both numerical and experimental analyses. It explores how float shape influences hydrodynamic performance and power absorption through a single degree of freedom in heave motion. To compare the dynamics of different floats under identical conditions, specific criteria were established. Using ANSYS AQWA for numerical modelling, two new float shapes—an asymmetric cylindrical wedge (HW) and an axisymmetric cone (CH)—were designed to match the natural frequency and mass of a conventional hemispherical-bottom (HB) float. Once these requirements were met, HW and CH floats were manufactured for experimental testing.**

The study investigates how variations in float geometry, particularly surface slopes at the waterline, affect hydrodynamic parameters and influence the response and power absorption of the Wave Energy Converter. Results show that the CH float, despite having the lowest peak response amplitude, achieved approximately 10% higher average absorbed power compared to the HB and HW floats, due to its broader bandwidth. The HW float exhibited the highest heave response amplitude overall. These findings highlight the critical role of radiation damping in power absorption and the importance of selecting suitable power take-off (PTO) damping.

Keywords—**Cone Hemisphere float, Float geometry, Radiation damping, Wave energy converter.**

Part of a special issue for AWTEC 2024. Manuscript submitted 20 February 2025; Revised 21 August 2025; Accepted 22 September 2025. Published 20 October 2025.

This research was supported by the Blue Economy Cooperative Research Centre through the project 'Seeding Marine Innovation in WA with a Wave Energy Deployment in Albany.' The Blue Economy Cooperative Research Centre (CRC) is established and supported under the Australian Government's CRC Program, grant number CRC-20180101.

R. Abbasi, J. Harris, L. Stedman, and T. Baldock are in the School of Civil Engineering, University of Queensland, St Lucia, QLD 4072, Australia (e-mail: r.abbasi@uq.edu.au).

Digital Object Identifier: https://doi.org/10.36688/imej.8.395-405

I. INTRODUCTION

Wave energy represents a promising renewable resource, particularly for islands and remote coastal regions. This potential is due to four key advantages: its global abundance, minimal environmental impact, predictability, and compatibility with other marine renewable technologies. In recent decades, the field of wave energy conversion has garnered significant attention due to the growing interest in renewable energy sources. Various energy conversion devices, including oscillating water columns (OWCs), point absorbers, attenuators, and overtopping devices, have been proposed[1]. WECs typically operate by harnessing the reaction forces between a wave-engaging body and a stationary structure fixed to the seabed [2]. Point-absorber converters like the PowerBuoy (a two-body floating system in which the float moves relative to a larger, moored reaction body that also floats. The relative motion between the two bodies is used to extract wave energy), WaveBob, Aquabuoy, IPS-buoy, FO3, and Uppsala University's Lysekil buoy use this technique [3].

Despite the advancements, many point-absorber WECs are still in the pre-commercial development stage, necessitating further optimization to reduce production costs and enhance efficiency. The effectiveness of these devices is influenced by the buoy motion and the operation of the power take-off (PTO) system [4]. Consequently, the design and behavior of the buoy are critical for optimizing wave energy absorption. Factors such as buoy shape, size, and the characteristics of incident waves play a significant role in determining the buoy response to waves. Optimizing buoy shape and dimensions has proven to be an effective method for improving converter efficiency [2, 5]. Additionally, optimizing the PTO system [6], submerged body geometry, and mooring system are important for enhancing PTO performance mechanisms [6].

Previous studies have explored various buoy shapes to assess WEC performance. Beirão and Malça [7] compared conical, spherical, and horizontal-cylindrical buoys, though variations in radius and mass led to non-identical conditions. Pastor and Liu [8] analyzed conical and hemispherical buoys with the same radius but differing masses under identical wave conditions. Using computer simulations, Backer et al. [9] studied a heaving point-absorber WEC with hemispherical and conical buoys of the same radius but different masses. These studies highlight the challenges in comparing buoy dynamics, specifically the effects of mass and radius on motion response, rather than the slope at the waterline. In contrast, Amiri et al. [10] compared four buoy shapes with equal mass but different radii, stressing the importance of maintaining consistent parameters such as mass and water-plane area to accurately compare buoy dynamics. Discrepancies in mass, wave characteristics, and buoy dimensions in earlier studies prevent direct comparison of their results. Nazari Berenjkoob et al. [11] conducted numerical investigations of different float shapes with the same natural frequency but varying sizes, analyzing dual motion and constant PTO damping. Ahmed et al. [12, 13] extended this work by exploring complex float shapes, also maintaining the same natural frequency and mass, to further understand their effects on wave energy converter (WEC) performance, focusing on complex construction shapes.

This study proposes a design approach based on incident wave properties to determine the optimal dimensions for a buoy to achieve the desired natural frequency and absorption bandwidth. By adjusting radiation damping, the buoy form is optimized to maximize energy absorption, fixing the mass and approximately maintaining the radius to preserve a constant natural frequency. Unlike previous research, this approach simultaneously considers three key parameters—mass, water-plane area, and natural frequency—along with experimental validation. The study introduces novel buoy shapes incorporating a slope on the water line and aims to identify critical hydrodynamic parameters necessary for designing an optimal buoy form based on wave characteristics. The novelty of this study lies in the systematic design and comparison of new float geometries with matched hydrodynamic conditions, combined with a focus on the role of waterline surface slope in enhancing radiation damping, and bandwidth—an aspect not previously addressed in comparable experimental–numerical frameworks.

II. METHODS

In this study, the dynamic behavior of the wave energy converter (WEC) in heave motion is analyzed using a time-domain model based on linear potential flow theory. The model captures the key hydrodynamic interactions by incorporating radiation damping, added mass, hydrostatic restoring force, and power take-off (PTO) damping. A single degree-of-freedom (1-DOF) system is assumed, focusing solely on vertical (heave) motion. This modelling approach is widely adopted in WEC studies due to its ability to capture energy extraction dynamics while remaining computationally efficient. The following sections present the governing equations of motion, the formulation of wave excitation force, and the calculation of natural frequency based on float geometry.

A. Governing equation and natural frequency

The governing equation of the WEC in heave, based on the second Newton law can be given as [14]:

$$(m + A_{33})\ddot{Z} + (B_{33} + B_{PTO})\dot{Z} + (K_{hys} + K_{PTO})Z = F_e \quad (1)$$

Here, m represents the mass of the buoy, A_{33} is the added mass coefficient, B_{33} is the radiation damping coefficient, B_{PTO} is the damping from the power take-off (PTO) system, K_{hys} is the hydrodynamic restoring coefficient, K_{PTO} is the PTO restoring coefficient, Z is the heave displacement, $\ddot{Z}$ is the acceleration, $\dot{Z}$ is the velocity, and F_e is the wave excitation force. The subscript 33 denotes the heave motion for a single degree of freedom. Accordingly, the mooring force is not included in Equation (1), since it had no influence on the vertical dynamics under investigation.

The wave excitation force based on the buoy's radiation damping coefficient (valid for axisymmetric bodies in deep water) according to Haskind's relation [15]:

$$F_e = \sqrt{\frac{2\rho g^3 B_{33}}{\omega^3}}\, a_\omega \quad (2)$$

where ρ is the water density, g is the acceleration due to gravity, ω is the wave frequency, and a_ω is the wave amplitude. Equation (2) demonstrates that the excitation force depends on the radiation-damping coefficient and the added mass of the buoy, indicating that variations in buoy shape can alter the wave excitation characteristics.

Assuming a constant diameter for cylindrical buoys, draft change is unavoidable when constructing different geometries. To induce resonance in buoy motion, a proper draft can bring the buoy's inherent frequency closer to the incident wave frequency [4]. When referring to identical mass, it implies that the submerged volume remains constant, though the draft of the float may vary. The primary assumption in buoy design is to maximize power capture from the incident waves. The natural heave frequency $\omega_{n_{33}}$ of the buoy can be calculated as follows [16]:

$$\omega_{n_{33}} = \sqrt{\frac{k_{hys}}{m + A_{33}}} = \sqrt{\frac{\rho g S_{wp}}{m + A_{33}}} \quad (3)$$

S_{wp} represents the buoy's water plane area. In line with existing literature, point-absorber WECs were also evaluated based on the buoy natural heave frequency, which is critical for efficiency [17-19].

According to (3) float shapes with equal mass (m) and restoring coefficients result in a similar natural frequency.

B. *Experimental calculation of radiation damping*

Equation (1) describes the motion of a heaving point absorber as a damped harmonic motion. Damping refers to the reduction of the energy of the body, which results in decreasing oscillation amplitude if exciting forces cease. Equation (1) specified the damping components as radiation damping and power take-off damping [20]. For a body in water, this damping will generate radial waves with an energy level proportional to the velocity of the body [21]. For a body with no power take-off and minimal viscous losses, this damping will be due to just radiation damping. Therefore, if two bodies with unequal radiation damping, but equal mass and waterline area are considered, if initially displaced, and released, the float with higher radiation damping should cease motion more quickly [20]. This type of test is known as a free decay test.

The method for calculating radiation damping from a free decay test begins by determining the rate of decay of amplitude, known as the damping ratio (ζ) [20].This parameter is applied to many structural, mechanical, and electrical systems. The damping ratio appears as a constant in the exponential decay term of the harmonic motion equation.

$$y = Ae^{-\zeta\omega_n t}\cos(\omega_n t - \emptyset) \tag{4}$$

where y represents the position of the body, A is the initial amplitude, $\emptyset$ describe the phase angle at time, t=0, and ω_n refers to the damped natural frequency of the body.

To calculate the damping ratio (ζ) from experimental free decay motion, it is recommended to calculate the log difference in height from two adjacent sets of maxima and minima (i.e., the peaks and troughs of the displacement time series) during a free decay test [20].This is expressed as:

$$\zeta = \frac{1}{2\pi}\ln\left(\frac{z_2 - z_3}{z_4 - z_5}\right) \tag{5}$$

where z_i denotes the elevations of the turning points during the free decay oscillation (see Figure 1).

The line passing through the turning points can be expressed as,

$$y = A_0 e^{-2\pi f\zeta} \tag{6}$$

Where, A_0 is the elevation at t=0, and f is the natural frequency of float during the free decay test.

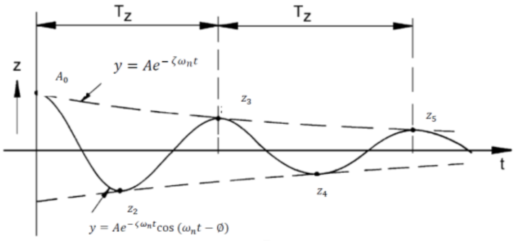

Figure 1 Estimating damping ratio from a free decay test [22].

The damping ratio can be related to radiation damping by considering some general definitions and rearranging terms. Firstly, damping ratio (ζ) is a non-dimensional ratio of actual damping c to critical damping c_{cr} [22].

$$\zeta = \frac{c}{c_r} \tag{7}$$

Critical damping is defined as the minimum damping coefficient which prevents oscillation. That is, after an initial excitation, the system will return to equilibrium in the shortest possible time without oscillating [22]. The general definition of critical damping is defined in terms of mass (m), and spring stiffness (k).

$$c_r = \sqrt{4mk} \tag{8}$$

By combining (7) and (8),

$$\zeta = \frac{c}{\sqrt{4mk}} \tag{9}$$

For a freely oscillating float (e.g., during a free decay), actual damping (c) is due to radiation damping (B_r [kg/s]) plus viscous damping. For large bodies, viscous damping is generally minor in comparison to radiation damping [20]. Furthermore, spring stiffness, k, is the hydrostatic stiffness (S [kg/s2]), and mass is the sum of gravitational mass and added mass (A [kg]). Equating these, reveal,

$$\zeta = \frac{B_r}{2\sqrt{s(m + A)}} \tag{10}$$

The mass term (m+A) can be calculated using a general harmonic equation relating mass, spring stiffness, and natural frequency.

$$m = \frac{k}{{\omega_n}^2} \tag{11}$$

In the case of an oscillating body in water, it yields,

$$m + A = \frac{S}{{\omega_n}^2} \tag{12}$$

By substituting (12) into (10), the damping ratio can be expressed as,

$$B_r = \frac{2\zeta S}{\omega_n} \tag{13}$$

Journée and Massie (2001) point out that this method only gives the radiation damping at one frequency, that is, the natural frequency. In practice, a wave absorber will be subject to a range of ocean wave states, with the radiation damping maximum at the natural frequency. To experimentally derive the hydrodynamic coefficients at other frequencies, a forced oscillation test can be completed. Journée and Massie (2001) recommend connecting the float to a cranking device, oscillating at a set frequency, and providing an amplitude governed by the radius of the crank. A pressure transducer will provide forcing which allows the calculation of radiation damping, added mass, and excitation forces [20].

C. *Power absorption and efficiency of WEC*

As seen in Figure 2, a damper and a spring connected in parallel serve as an example of the PTO system (It may not be seafloor-connected).

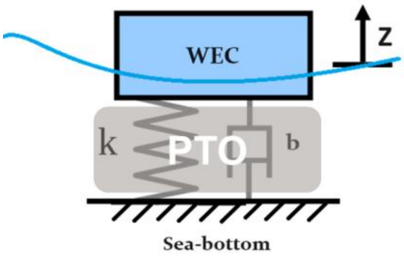

Figure 2 Schematic of the WEC float under the heave motion

The buoy's power absorption and hydrodynamic response are strongly influenced by the power take-off damping coefficient (B_{PTO}) and spring stiffness (K_{PTO}). The floating buoy's absorbed power can be computed as follows [23] :

$$P_a = \frac{1}{T}\int_0^T B_{PTO}u^2 dt = \frac{1}{2}B_{PTO}\omega^2\left|\hat{Z}\right|^2 \tag{14}$$

where Z is the total heave displacement of the buoy and ω is the wave frequency.

By substituting the displacement of the device (float) with the complex amplitude, into (1) the following expression is obtained [23]:

$$P_a = \frac{1}{2}\frac{B_{PTO}\omega^2\left|\hat{F}_e\right|^2}{\left[-\omega^2(m+A)+K_{PTO}+K_{hys}\right]^2 - \omega^2(B+B_{PTO})^2} \tag{15}$$

The frequency-domain analysis of the floating buoy determines the radiation damping B and added mass A. The power absorbed by the PTO can be related to the excitation forces acting on the heaving buoy ($\hat{F}_e$), radiation damping, and B_{PTO} and K_{PTO} [24].

For some simple geometries, simple expressions for the maximum capture width in deepwater conditions exist, particularly for a heaving axisymmetric body [25]:

$$L_{max} = \frac{\lambda}{2\pi} = \frac{gT^2}{4\pi^2} \tag{16}$$

By substituting the maximum power that is available in the regular waves to be absorbed by an axisymmetric oscillating resonant buoy can be given by [13]:

$$P_{max} = \frac{\rho g^3 H^2}{32\omega^3} \tag{17}$$

The capture width ratio (CWR), which is a measure of the wave energy absorption efficiency normalized by the buoy diameter, describes the performance of the WEC [24]:

$$CWR = \frac{P_a}{P_{max} \times D} \times 100 \tag{18}$$

where D is the effective length of a WEC, which refers to the diameter of the float in a point absorber.

III. DESIGN AND MODELLING OF NEW FLOATS

In this study, a float shape with a hemispherical bottom (HB) will be used as a reference for an oscillating body. Various float shapes, specifically those featuring a slope at the waterline, will be investigated while keeping factors such as natural frequency and mass constant. The objective is to compare these shapes to assess changes in the power absorption capability of the heaving device, an aspect not addressed in previous literature. Consequently, various float shapes were selected. The first buoy had a cylindrical shape with a semi-hemispherical bottom, similar to the float designs of various point absorbers like WaveStar. The other designs featured a sloped waterline (both asymmetric and symmetric) to experiment with different shapes. The goal was to find a shape with the same submerged volume (mass of the float) and control the mass by changing the draft and shape of the submerged part, which directly affects the natural frequency (refer to (2) and (3)).

Additionally, this investigation aimed to keep the water plane area consistent across all designs to maintain the natural frequency by controlling the mass and hydrostatic coefficient. The concept behind selecting different float shapes is rooted in the hydrodynamic coefficients which all affect the power absorption ability and response of floating objects against incoming waves. When discussing float shapes, various parameters such as volume, mass, draft, and other characteristics can influence the overall design. Based on Equation 3, the natural frequency is influenced by factors such as hydrostatic stiffness, mass, and added mass of the float. By fixing certain parameters and varying the float shapes, the goal is to identify the optimal shapes that meet these requirements.

TABLE 1 FLOATS DIMENSIONS AND IMAGES

Float name	**Float dimensions (mm)**	**Draft (mm)**	**Manufactured model**
Hemisphere bottom **(HB)**	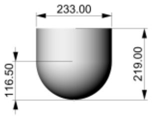	153	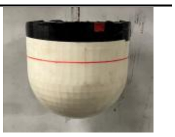
Half Wedge **(HW)**	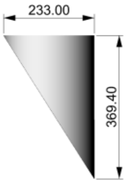	294	
Cone Hemisphere bottom **(CH)**	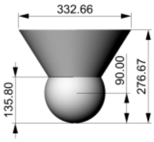	207	

Based on the requirements and input wave characteristics, such as a specific sea state, and float shapes were selected, depicted in Table 1 (Considering that the slope on both the HW and CH floats is equal.). Both physical and numerical models were developed within that range of wave characteristics.

As depicted in Figure 3, once the numerical model of the new CAD design demonstrated feasibility within the specified criteria, a physical model was prepared, and experimental analysis commenced. This approach was repeated multiple times, ultimately resulting in the selection of two distinct float shapes. The natural frequency of each float shape was determined by identifying the peak of their response in a wave.

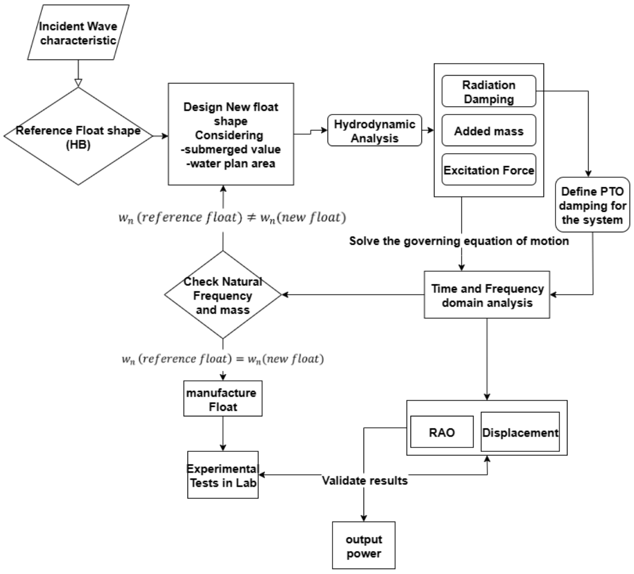

Figure 3 Flowchart of design and physical and numerical analysis of present work

In the initial step of these models, it was necessary to determine the hydrodynamic coefficients. Subsequently, the device's response was analysed in both the time and frequency domains. For the present research, the hydrodynamic coefficients were calculated using the AQWA Ansys package software. The original shape featured a semi-hemispherical bottom. As shown in **Error! Reference source not found.**, all characteristics, such as natural frequency, mass (submerged volume), and stiffness, were considered when selecting new float shapes.

TABLE 2 SPECIFICATION OF DIFFERENT FLOATS

Float name	**Mass (kg)**	**Submerged volume (m^3)**	**Water plane area (m^2)**	**Draft (mm)**	**Natural Frequency (Hz) (numerical predicted)**
HB *(Hemisphere bottom)*	4.94	$4.81{\times}10^{-3}$	$4.24{\times}10^{-2}$	153	1.27
HW *(Half wedge)*	4.96	$4.84{\times}10^{-3}$	$3.82{\times}10^{-2}$	294.40	1.26
CH *(Cone Hemisphere)*	4.91	$4.79{\times}10^{-3}$	$4.67{\times}10^{-2}$	206.66	1.31

Two additional float shapes were chosen, focusing on the slope of the body. This iterative process involved designing new CAD models and performing numerical modelling to find a shape that aligns with the original one. The alignment is based on submerged volume (mass) and water plane area, which directly affect the natural frequency. Throughout this process, factors such as submerged volume, water plane area, stiffness, and natural frequency were kept constant, and the shape was modified within these constraints. However, even small differences in the water plane area can directly affect the natural frequency.

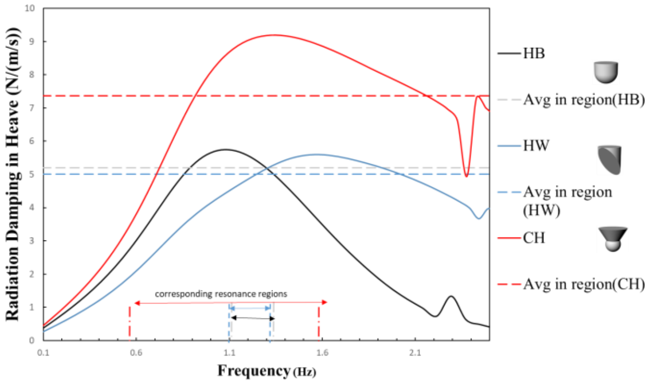

Figure 4 Radiation damping of different float shapes in heave, and their average in the corresponding resonance regions for defining PTO damping

After identifying two appropriate shapes that met the criteria, numerical analysis was performed for heave motion to determine which float shape could absorb more power with its specific PTO damper.

The amount of PTO damping was selected based on the corresponding resonance frequencies for radiation damping in heave [26], and the optimum was chosen by averaging these frequencies, as depicted in Figure 4. The cone shape CH has greater radiation damping and over a broader range of frequencies.

IV. EXPERIMENTAL SETUP

The experiments were undertaken at the University of Queensland hydraulics laboratory. The wave flume (22.5 m x 2 m x 0.960 m deep) was equipped with a DHI paddle wave system. Figure 5 displays a diagram of the setup used for all experimental tests. Figure 6 and Figure 7 are images of the setup.

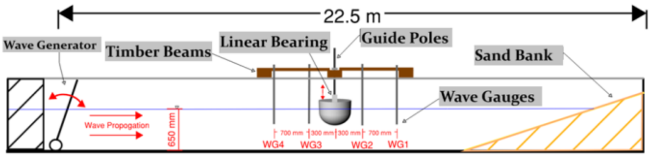

Figure 5 Elevation Diagram of the Experimental Setup (not to scale)

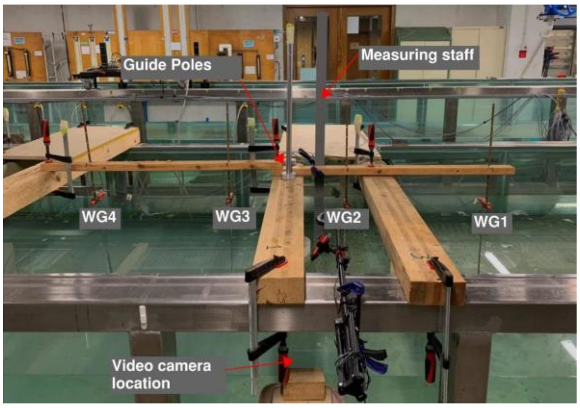

Figure 6 Apparatus layout – wave direction from left

A structure consisting of four beams across the flume and two additional beams longitudinally was created to mount equipment. This was situated at approximately the midpoint of the length of the flume. The structure included two circular tube sections (poles) mounted vertically which guided the float in heave and prevented oscillation in other modes (see Figure 7). Four 201/65 DHI wave gauges were mounted longitudinally along the tank, on either side of the float. Wave reflection effects were considered during the experimental tests. To minimize reflections, a sand bank with a gentle slope was installed at the end of the flume, acting as a natural wave absorber (see Figure 5). Positions of the wave gauges, relative to the centreline of the float and dimensioned on Figure 5. A measuring staff was installed to measure the displacement of the floats and provide a calibration for video tracking. A platform to mount a mobile phone for video recording was set up on the outside of the flume panel, at the elevation of the float, to achieve a planar view. Figure 7 provides the typical footage captured during free decay and incident wave trials.

Figure 7 Example of footage captured for free decay and incident wave tests

D. *Free decay test*

A free decay test was conducted to i) measure the natural frequency of the floats to inform an expected resonance frequency during incident wave tests, ii) calculate radiation damping based on the motion decay of the float, and iii) measure the waves generated by the body to infer radiation damping.

The apparatus was set up as outlined in Figure 5. Each float was attached to the guide poles and tested separately. To initiate the free decay test, the float was slowly displaced from equilibrium and held steady for several seconds, followed by sudden release. Six free decay tests were performed per float. Three trials involved displacing the float downwards (pushing) and releasing, and three trials involved displacing the float upwards (lifting) and releasing. These trials will later be referred to as 'push' and 'lift'. The magnitude of displacement for these trials was approximately 50 to 80 mm. Wave gauges measured the height of waves caused by the disturbance, and a video recorded the motion of the float at 60 frames per second. This framerate was determined sufficient as the error would be approximately 1/60 seconds for determining the natural frequency. This amounts to 1.1% error considering the lowest numerically predicted natural period (cone at 0.76 seconds).

Figure 8 displays a comparison of free decay motion of the three floats released at approximately 70 mm above their equilibrium position. Six trials were conducted for each float; however, the results displayed in Figure 8 are representative of the majority.

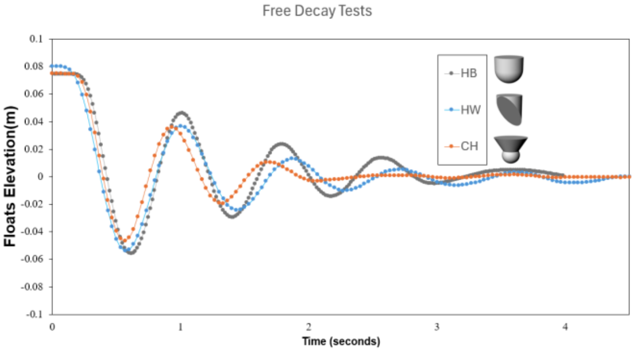

Figure 8 Free decay motion: comparison between floats released at the same height. These trials are representative of the majority of the trials conducted.

Table 3 Experimental natural frequency compared to the numerical prediction

Float shape	Experimental Natural Frequency [Hz]	Numerical Natural Frequency [Hz]
HB	1.28	1.27
HW	1.18	1.26
CH	1.33	1.31

Table 3 shows the experimental natural frequencies and the numerical natural frequencies of each float. The experimental natural frequency was calculated by considering the time difference between the initial turning points of the decay motion plot. After 3 – 4 oscillations the motion stopped completely or became irregular due to the bearings ‘sticking’ to the poles at low velocity. The experimental results agree well with the numerical model, with less than 2% relative error for the hemisphere and cone, and 6.5% for the truncated or half wedge cylinder. The larger error for the truncated cylinder is a reflection of its lower mass in the experiments compared to the numerical model.

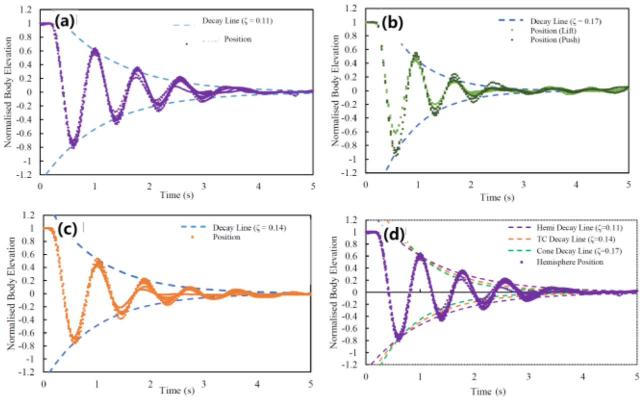

Figure 9 a) HB float: normalized free decay for six trials – $\zeta = 0.11$ b) CH float: normalized free decay for six trials - $\zeta = 0.17$. Differences between push and lift trials were significant for the cone float. c) HW Float: Normalised free decay for six trials- $\zeta = 0.14$ d) Hemisphere normalized cone elevation compared to the decay line of all floats

Figure 9 show the normalized body elevation of the floats during free decay tests, with data for 6 trials displayed in each. The float elevation data for each trial was normalized by the initial displacement (i.e., the height it was released) for that respective trial. This allowed free decays of differing release displacement to be compared, assuming the rate of decay is approximately constant regardless of release displacement. This assumption appeared valid for the hemisphere and half wedge floats based on the relatively low variance of the curves in Figure 9 (a and c). It became clear that there were differences between trials where the cone was pushed and released, as opposed to lifted and released. Therefore, Figure 9 (b) makes a distinction between these.

The damping ratio (ζ) was calculated based on the decay in motion, as described by (13). For each float, the damping ratio was calculated separately for each trial. Figure 9 (b) to Figure 10, Table 4 display the mean damping ratio. A decay line with a function described by (6), has been plotted in the figures. It shows a decent fit to the experimental data. To demonstrate the sensitivity of the decay slope to the damping ratio, Figure 9 (d) plotted the hemisphere decay data aside the decay line for all float shapes. It shows a noticeably worse fit of the HW and CH decay line to the hemisphere data.

Table 4 Experimental results for mean damping ratio (Z), radiation damping ($\boldsymbol{B_r}$), added mass, ($\boldsymbol{A}$), and excitation force ($\boldsymbol{Fe}$)

Float shape	Damping Ratio	Radiation Damping [kg/s]	Added Mass [kg]	Excitation Force [N]
HB	0.11	11.4	1.54	128.03
HW	0.14	14.2	2.04	161.31
CH	0.17	18.6	1.65	154.70

Table 4 displays hydrodynamic parameters calculated based on the free decay motion. Radiation damping was calculated using the experimental damping ratio and natural frequency, as per (13). This method assumed the motion to be that of a damped linear spring, where the spring stiffness is equal to the hydrostatic stiffness. Added mass was calculated as a function of hydrostatic stiffness and experimental natural frequency, as described by (12). Excitation force was calculated using Haskins relation (2) which was a function of radiation damping, wave frequency, and wave height.

The results indicate the cone had the greatest radiation damping and the hemisphere had the least. To validate the significance of the difference in the mean damping ratio of the floats, the samples of damping ratios gathered from 6 trials for each float were analyzed with a *t*-test. Results of the *t*-test analysis found statistically significant differences between means for the hemisphere and truncated cylinder test (p=.027), the HW float and CH float (p=.031), and the HB and CH (p<.001). Therefore, the mean damping ratios displayed in Figure 9 and Figure 10 and Table 4 were considered statistically valid and representative of the difference in rate of decay among the floats.

Figure 10 (a, b and c) compare the experimentally derived hydrodynamic parameters to values numerically calculated with hydrodynamic diffraction analysis (AQWA).

Figure 10 (a) shows both numerical and experimental results indicate the cone has higher radiation damping than the other floats. However, the magnitude of experimental radiation damping ratios was significantly higher, likely due to additional damping from the bearings. Additionally, the numerical model predicted a very similar radiation damping between the cone and hemisphere at their respective natural frequency, whereas the experimental results indicate a greater distinction between the two floats. Figure 10 (b) illustrates the added mass comparison between numerical and experimental results. The experimental data corresponds to tests conducted at a single wave frequency specific to each float. Overall, there is good agreement between the numerical predictions and experimental measurements. The added mass values for all floats lie within a similar range, and the experimental results follow a consistent and acceptable trend, validating the numerical model.

Figure 10 (c) presents the excitation force amplitude, showing that both numerical and experimental results follow a similar trend. Notably, the hemisphere float lies between the other two float types in both data sets, indicating strong agreement between the model and the physical observations.

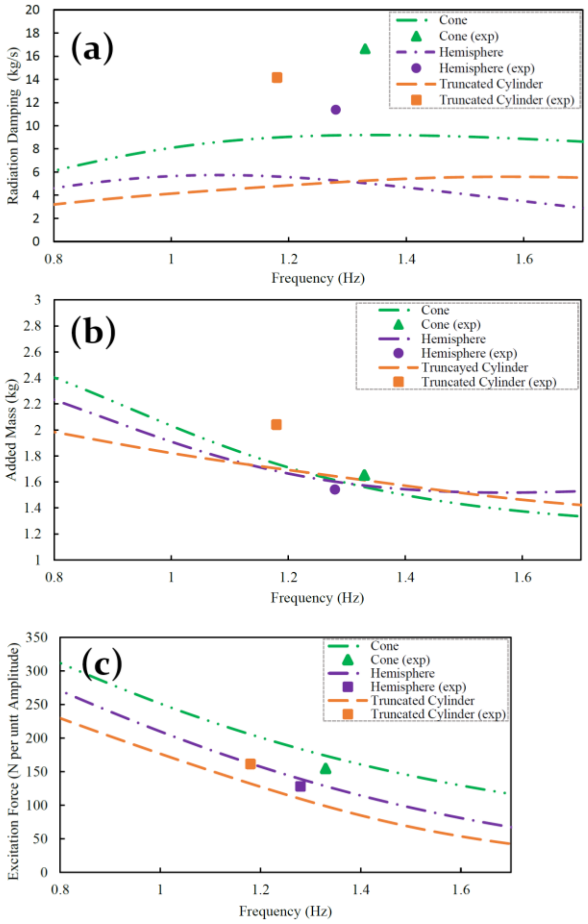

Figure 10 Numerical versus experimental (exp) Results a) Radiation damping b) Added mass c) Excitation force

In all subfigures, Figure 10(a), (b), and (c), the deviation of the truncated cylinder float from the other two floats can be attributed to its slightly different natural frequency, which affects its hydrodynamic response.

Aside from the comparison of hydrodynamic coefficients, the numerical and experimental comparisons of the displacement of different floats showed good agreement. By comparing the simulation results with time-domain analysis from wave flume tests performed under various incident waves, the simulation study carried out in ANSYS AQWA was validated. Figure 11 plots the displacement of the heaving buoy over time for various incident wave frequencies. With the exception of a few frequencies that were close to the natural frequency, where differences could have been caused by the accuracy constraints of frequency-domain analysis, it was found that the simulation results and the trials agreed fairly well given an unknown resistance in the bearings.

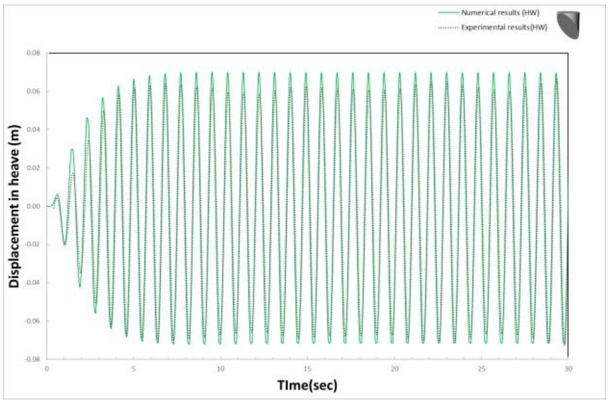

Figure 11 Comparison of float considering heave response under identical design and test parameters (regular waves characterized by 0.02 m wave height and 1.11 Hz frequency).

V. INCIDENT WAVE RESPONSE RESULTS

The response amplitude operator (RAO) of the floats at the range of tested frequencies is summarised in Figure 12. The results show the HW float had the greatest heave response amplitude of all frequencies, due to its asymmetric shape and hydrodynamic coefficients, followed by the HB float, and the CH float with the lowest response amplitude. The general shape and magnitude of peak RAO agree with the numerical prediction.

After validating the results in both the time and frequency domains, it is necessary to define a power take-off (PTO) system based on the average radiation damping of each float, as presented in Figure 4, and calculate the absorbed power under the same wave conditions using (15). Additionally, the maximum power available in the waves can be calculated using (18). As shown in Figure 13, the black line represents the maximum power for the current wave condition simulation, while the other lines illustrate the power absorption of different heaving point absorbers with various float shapes. It shows that the CH float shape's capacity to absorb power is particularly significant compared to the other two shapes, as its wider bandwidth allows it to absorb power across a broader frequency range.

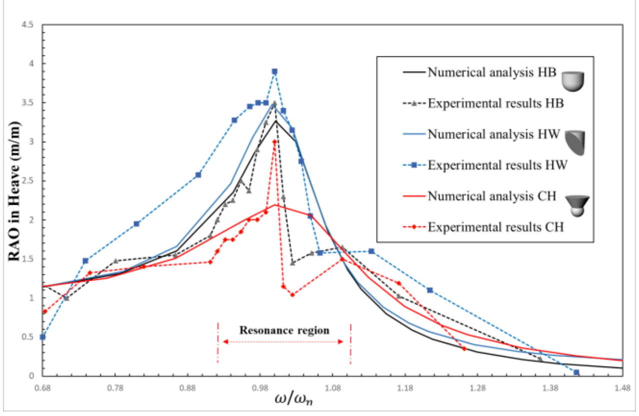

Figure 12 Comparison normalized heave RAO of experimental and numerical (frequency domain) analysis. No PTO damping in the system.

After validating the results in both the time and frequency domains, it is necessary to define a power take-off (PTO) system based on the average radiation damping of each float, as presented in Figure 4, and calculate the absorbed power under the same wave conditions using (15). Additionally, the maximum power available in the waves can be calculated using (18). As shown in Figure 13, the black line represents the maximum power for the current wave condition simulation, while the other lines illustrate the power absorption of different heaving point absorbers with various float shapes. It shows that the CH float shape's capacity to absorb power is particularly significant compared to the other two shapes, as its wider bandwidth allows it to absorb power across a broader frequency range.

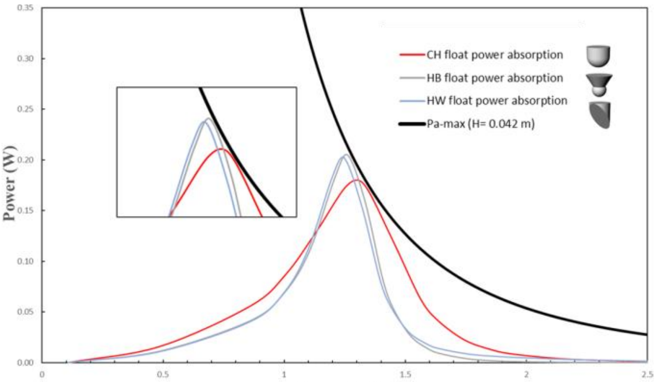

Figure 13 Power absorption of various floats compared to the highest power absorbed over several frequency ranges.

To provide a clearer comparison of the floats' power absorption abilities, normalizing their performance based on their natural frequencies is useful. allowing for a fair comparison across different float types. Figure 14 shows that although the maximum power absorbed by the CH float is less than that of the HB and HW floats, its bandwidth over the range of normalized frequencies is wider.

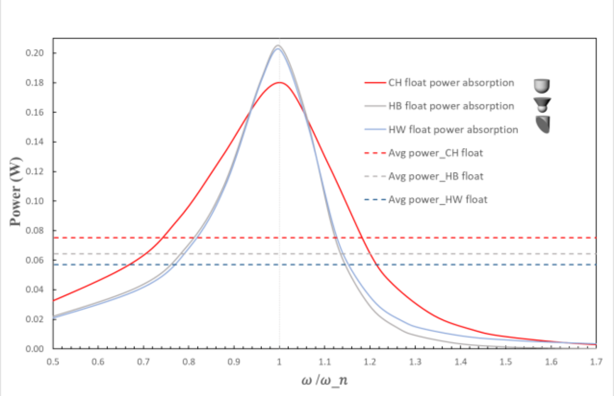

Figure 14 Normalized power absorption using natural frequency and frequency range average.

This characteristic highlights the advantage of float shapes with a surface slope at the waterline on their bodies, which significantly increases radiation damping. Another comparison involves evaluating the amount of absorbed power independently of the maximum available power in the wave. The average absorbed power over the range of normalized frequencies, which is the same for all float shapes, is shown in Figure 14. The average power for the CH float is approximately 10 percent higher than that of the other two floats, which is attributed to its wider bandwidth. This highlights an important factor to consider when comparing different wave energy converters (WECs): their power absorption ability under various wave conditions. Key aspects include having a broader absorption bandwidth or maximizing absorption at specific frequencies.

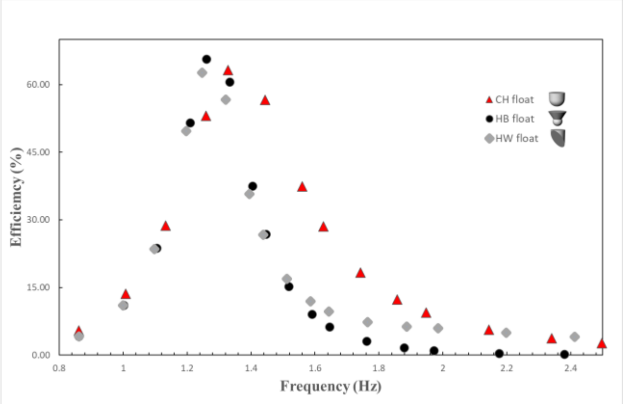

Figure 15 Comparison of the efficiency of different float shapes in a range of frequency

Another method to compare the performance of wave energy converters is the capture width ratio (CWR), which measures wave energy absorption efficiency normalized by the buoy diameter. By considering the diameter of different floats in the water plane area—where there are slight differences as shown in **Error! Reference source not found.**—and using (18) to determine the maximum available power in the incoming wave, the efficiency of different heaving point absorbers with various float shapes can be calculated using (19).

As illustrated in Figure 15, the efficiency of the CH float, particularly at frequencies greater than the natural frequency, is significantly higher than that of the other two floats, despite having a lower maximum power compared to the HB float. This may be beneficial for random seas states where there is significant energy in the wave spectrum for $f > f_P$.

Figure 16 shows that the efficiency of different float shapes, normalized by their natural frequency, is approximately equal at their natural frequencies, which corresponds to the peak of the graph. This similarity is due to the small differences in the natural frequencies of the CH float compared to the other two floats, which are 1.31 and 1.27, respectively. This small difference pulls the absorption power diagram under the lower available maximum power in the wave, as shown in Figure 14. The variation in efficiency is primarily attributed to the wider bandwidth of the HW and CH floats, which is related to their higher radiation damping, as indicated in Figure 4, and the excitation force shown in Figure 11 (with the added mass of the floats being approximately in the same range).

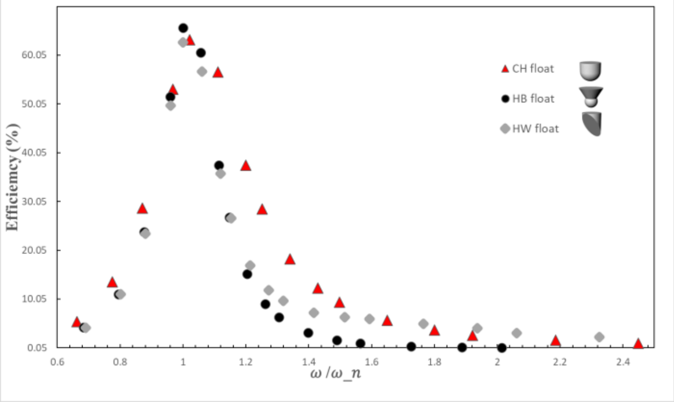

Figure 16 Comparison of the efficiency of different float shapes normalised by natural frequency

Higher efficiency becomes more apparent at higher frequencies. Comparing floats with equal mass and approximately similar natural frequencies highlights the importance of selecting floats with different hydrodynamic coefficients, especially radiation damping, which is closely related to the amount of PTO damping. It is also crucial to consider the impact of PTO damping on the power absorption of WECs, as it significantly influences their performance.

VI. CONCLUSION

This study investigated the hydrodynamic performance of different float shapes for heaving point absorber wave energy converters (WECs) through numerical modeling and experimental validation. The Response Amplitude Operator (RAO) analysis revealed that the HW float exhibited the highest heave response amplitude across the tested frequency range, followed by the HB and CH floats. These findings were consistent with the numerical predictions, demonstrating the reliability of the developed model.

Power absorption analysis showed that the CH float, despite having the lowest peak response amplitude, exhibited a wider bandwidth of power absorption compared to the HB and HW floats. This broader bandwidth translated into approximately 10% higher average absorbed power over the normalized frequency range, emphasizing the advantage of float shapes with surface slopes at the waterline that enhance radiation damping. The normalized efficiency of the floats was similar near their natural frequencies; however, the CH and HW floats displayed higher efficiencies at elevated frequencies, primarily due to their increased radiation damping and excitation force characteristics.

The results highlight the critical role of float geometry and hydrodynamic coefficients—especially radiation damping—in maximizing energy capture in WECs. Moreover, the study underscores the importance of optimizing power take-off (PTO) damping in conjunction with float design to enhance device performance. Future work should focus on further refining the numerical model by incorporating mechanical losses such as bearing friction to better match experimental radiation damping results. Expanding experimental testing across a wider range of wave frequencies and sea states will help validate the model's robustness under diverse conditions. Additionally, investigating optimized float geometries and PTO damping strategies could enhance power absorption efficiency and broaden operational bandwidths.

VII. ACKNOWLEDGMENT

The authors would like to thank Jason Van Der Gevel for his assistance in constructing the model and facilitating the experiment at the University of Queensland.

REFERENCES

1. Abbasi, R. and M.J. Ketabdari, *Enhancement of OWC Wells turbine efficiency and performance using riblets covered blades, a numerical study.* Energy Conversion and Management, 2022. **254**: p. 115212.
2. Viet, N.V., et al., *Energy harvesting from ocean waves by a floating energy harvester.* Energy, 2016. **112**: p. 1219-1226.
3. Pietra, L., et al., *Review and classification of wave energy converters.* Centre for Marine Technology and Engineering (CENTEC), Instituto Superior Técnico, Lisboa, Portugal. doi, 2012. **10**.
4. Chen, Z., et al., *Performance evaluation of a dual resonance wave-energy convertor in irregular waves.* Applied Ocean Research, 2018. **77**: p. 78-88.
5. Shadman, M., et al., *A geometrical optimization method applied to a heaving point absorber wave energy converter.* Renewable Energy, 2018. **115**: p. 533-546.
6. Li, X., et al., *Optimum power analysis of a self-reactive wave energy point absorber with mechanically-driven power take-offs.* Energy, 2020. **195**: p. 116927.
7. Beirão, P.J.B.F.N. and C.M. dos Santos Pereira Malça, *Design and analysis of buoy geometries for a wave energy converter.* International Journal of Energy and Environmental Engineering, 2014. **5**(2): p. 91.
8. Pastor, J. and Y. Liu, *Frequency and time domain modeling and power output for a heaving point absorber wave energy converter.* International Journal of Energy and Environmental Engineering, 2014. **5**(2): p. 101.
9. De Backer, G., et al., *Bottom slamming on heaving point absorber wave energy devices.* Journal of Marine Science and Technology, 2010. **15**(2): p. 119-130.
10. Amiri, A., R. Panahi, and S. Radfar, *Parametric study of two-body floating-point wave absorber.* Journal of Marine Science and Application, 2016. **15**(1): p. 41-49.
11. Berenjkoob, M.N., M. Ghiasi, and C.G. Soares, *Influence of the shape of a buoy on the efficiency of its dual-motion wave energy conversion.* Energy, 2021. **214**: p. 118998.
12. Ahmed, A., et al., *On the S-shaped floaters for a Wavestar-like wave energy converter with an I-shaped mechanical power take-off.* Energy Conversion and Management: X, 2023. **19**: p. 100387.
13. Ahmed, A., et al., *Design and analysis of the bulbous-bottomed oscillating resonant buoys for an optimal point absorber wave energy converter.* Ocean Engineering, 2022. **263**: p. 112443.
14. Falnes, J., *Ocean Waves and Oscillating Systems: Linear Interactions Including Wave-Energy Extraction*. 2002, Cambridge: Cambridge University Press.
15. Newman, J.N., *Marine hydrodynamics*. 2018: The MIT press.

16. Joe, H., et al., *Development of a flap-type mooring-less wave energy harvesting system for sensor buoy.* Energy, 2017. **133**: p. 851-863.
17. Jin, P., et al., *Performance optimization of a coaxial-cylinder wave energy converter.* Energy, 2019. **174**: p. 450-459.
18. Piscopo, V., et al., *A new optimization procedure of heaving point absorber hydrodynamic performances.* Ocean Engineering, 2016. **116**: p. 242-259.
19. Vantorre, M., R. Banasiak, and R. Verhoeven, *Modelling of hydraulic performance and wave energy extraction by a point absorber in heave.* Applied Ocean Research, 2004. **26**(1): p. 61-72.
20. Journée, J. and W. Massie, *Offshore hydromechanics.* Delft University of Technology, 2001.
21. Todalshaug, J.H., *Hydrodynamics of WECs*, in *Handbook of Ocean Wave Energy*, A. Pecher and J.P. Kofoed, Editors. 2017, Springer International Publishing: Cham. p. 139-158.
22. Inman, D.J., *Vibration with control*. 2017: John Wiley & Sons.
23. Shi, H., S. Huang, and F. Cao, *Hydrodynamic performance and power absorption of a multi-freedom buoy wave energy device.* Ocean Engineering, 2019. **172**: p. 541-549.
24. Azam, A., et al., *Design and analysis of the optimal spinning top-shaped buoy for wave energy harvesting in low energy density seas for sustainable marine aquaculture.* Ocean Engineering, 2022. **255**: p. 111434.
25. Evans, D.V. and R. Porter, *Wave energy extraction by coupled resonant absorbers.* Philosophical Transactions: Mathematical, Physical and Engineering Sciences, 2012. **370**(1959): p. 315-344.
26. Falnes, J. (2007). *A Review of Wave-Energy Extraction*. Marine Structures, 20(4), 185–201.